Available online at www.sciencedirect.com
ScienceDirect
Comput. Methods Appl. Mech. Engrg. xxx (xxxx) xxx
Computer methods in applied mechanics and engineering
www.elsevier.com/locate/cma

Highlights

A FIC-FEM procedure for the shallow water equations over partially wet domains

Miguel Masó*, Ignasi de-Pouplana, Eugenio Oñate

Comput. Methods Appl. Mech. Engrg. xxx (xxxx) xxx

- A numerical method for solving shallow water problems with the FEM is presented.
- The new algorithm is based on stabilization of FEM with FIC.
- The presented FIC-FEM procedure is able to design a shock capturing technique.
- The algorithm is able to solve shallow water problems on partially wet domains.
- Several cases have been analyzed to validate the method.

Please cite this article as: M. Masó, I. de-Pouplana and E. Oñate, A FIC-FEM procedure for the shallow water equations over partially wet domains, Computer Methods in Applied Mechanics and Engineering (2021) 114362, https://doi.org/10.1016/j.cma.2021.114362.

CMA: 114362

ARTICLE IN PRESS

Available online at www.sciencedirect.com

ScienceDirect

Comput. Methods Appl. Mech. Engrg. xxx (xxxx) xxx

Computer methods in applied mechanics and engineering

www.elsevier.com/locate/cma

A FIC-FEM procedure for the shallow water equations over partially wet domains

Miguel Masó*, Ignasi de-Pouplana, Eugenio Oñate

Centre Int. de Mètodes Numèrics a l'Enginyeria (CIMNE), Barcelona, Spain
Universitat Politècnica de Catalunya (UPC), Barcelona, Spain

Received 22 May 2021; received in revised form 11 November 2021; accepted 14 November 2021
Available online xxxx

Abstract

We present a stable finite element formulation for the shallow water equations using the finite increment calculus (FIC) procedure. This research is focused on the stability properties of the FIC technique and uses linear triangles for the spatial discretization with an equal order of interpolation for all the variables. The extension to higher order polynomial interpolation functions and different geometries is straightforward. The present FIC-FEM procedure is also able to introduce artificial viscosity for an adequate shock capturing. An implicit time integration has been used. Special attention has been payed to the dry domain in order to solve the moving boundaries with a fixed mesh eulerian approach. Three academic examples are included in order to test the capabilities of the FIC-FEM procedure: the global stabilization, the shock capturing technique and the dry-wet interface. An experimental benchmark tests the overall accuracy of the present formulation.

Keywords: Shallow water equations; Finite element method; Continuous Galerkin; FIC stabilization; Dry-wetting model

1. Introduction

The shallow water equations are often used to study the hydrological dynamics of rivers and estuaries or coastal hydrodynamics. Derived from the vertical integration of the three-dimensional (3D) Navier–Stokes equations, the shallow water equations define an averaged free surface flow in the horizontal plane. Due to the complexity of the geometry and the source terms is not possible to find an analytical solution for the PDE's, this explains the need to design strategies to find numerical solutions. In those physical phenomena, flooding or moving shoreline may occur, which is numerically defined by a null water depth.

The shallow water equations have traditionally been modelled using finite volumes (FV) because of its advantages of stability and monotonicity. Given its geometric flexibility and its natural way to introduce high order schemes, the finite element method (FEM) has been applied too [1–3]. However, since the FEM can exhibit spurious oscillations, different strategies such as stabilization, monotonic schemes or different order of polynomial interpolation can be explored [1,4,5]. As an alternative to the continuous FEM, more recently the discontinuous Galerkin (DG) technique has been introduced [6–8]. DG method has the advantages of the geometrical flexibility of the FEM and the stability of FV, but the introduction of high order DG schemes is not straightforward. This research is focused in classical

* Corresponding author at: Centre Int. de Mètodes Numèrics a l'Enginyeria (CIMNE), Barcelona, Spain.
E-mail address: mmaso@cimne.upc.edu (M. Masó).

https://doi.org/10.1016/j.cma.2021.114362
0045-7825/

stabilized finite elements with an equal order interpolation for all the variables. We will explore the capabilities of the finite increment calculus (FIC) technique to develop stable formulations for the shallow water equations.

Several families of stabilization methods can be found in the literature, usually applied to the convection–diffusion equations and the Navier–Stokes equations. The most relevant are SUPG [9], ASGS [10], GLS [11] and FIC [12,13]. Due to the hyperbolic character of the shallow water equations, a particular stabilization method for compressible flow or the Euler equations need to be developed. The FIC approach is based on the incremental solution of a modified system of non-local governing equations accounting for higher order terms obtained by applying the balance laws in domains of finite size. The FIC-based stabilization has been applied in conjunction with the FEM to convection–diffusion, incompressible flows, among other applications [13,14]. In those cases, where the convective term has an important role, a first order FIC term is enough to provide stability to the system. However, the shallow water equations are governed by the convective term and the wave equation in a mixed formulation [15]. In consequence, the common derivation of the FIC-based stabilization is not enough to provide stability in all the range of applicability of the shallow water equations. A generalization of this method is proposed in order to provide a global stability for the shallow water equations.

Once global stability is achieved, local instabilities may appear near discontinuities, which are inherent to the supercritical flows. A local shock capturing technique was initially proposed by Hughes [16] and a review of shock capturing techniques can be found in Codina [17]. Other possibilities of the FIC-based formulations are explored to provide a shock capturing stabilization [18].

Additionally, the dry domain requires an accurate modeling because the hyperbolic equations require positive water depth in all the domain. Several authors have proposed different methods to solve the shallow water equations with moving shoreline. Leclerc et al. [19] proposed an Eulerian method. Later, Heniche et al. [20] modified the method allowing the free surface to plunge under the topography. Other authors developed a rough-porous layer [21,22] or a modified depth integration [23]. These approaches introduce new physical parameters in the balance equations. An Eulerian approach based on the work of [19,20] is presented.

This article is organized as follows. Firstly the governing equations of the shallow water problems are presented. In Section 3 the FIC stabilization procedure is applied to add the stabilization terms and the shock capturing terms. In Section 4 the spatial (FEM) and temporal discretizations are described. The dry domain model is presented in the same section because it mainly depends on the discretization. Section 5 presents some numerical examples. The first simple example tests the stability, the second one tests the dry-wet interface and the third one tests the shock capturing. The last example is a simulation of an experiment and the results are compared with the reference. The conclusions are given in Section 6.

2. Governing equations and linearization

The shallow water equations are the result of integrating vertically the Navier–Stokes equations, assuming the vertical velocity and its acceleration negligible [1,24]. The equations governing mass and momentum conservation can be written in conservative form with water depth h and specific discharge $\mathbf{q} = (h\mathbf{u})$ as follows,

$$\frac{\partial \boldsymbol{\phi}}{\partial t} + \frac{\partial \mathbf{F}_i}{\partial x_i} + \frac{\partial \mathbf{G}_i}{\partial x_i} + \mathbf{Q} = \mathbf{0} \quad \text{for} \quad i = 1, 2 \tag{1}$$

with

$$\boldsymbol{\phi} = \begin{Bmatrix} hu_1 \\ hu_2 \\ h \end{Bmatrix} \tag{2a}$$

$$\mathbf{F}_i = \begin{Bmatrix} hu_1u_i + \delta_{1i}\frac{1}{2}g(h^2 - z^2) \\ hu_2u_i + \delta_{2i}\frac{1}{2}g(h^2 - z^2) \\ hu_i \end{Bmatrix} \tag{2b}$$

$$\mathbf{G}_i = \begin{Bmatrix} -(h/\rho)\bar{\tau}_{1i} \\ -(h/\rho)\bar{\tau}_{2i} \\ 0 \end{Bmatrix} \tag{2c}$$

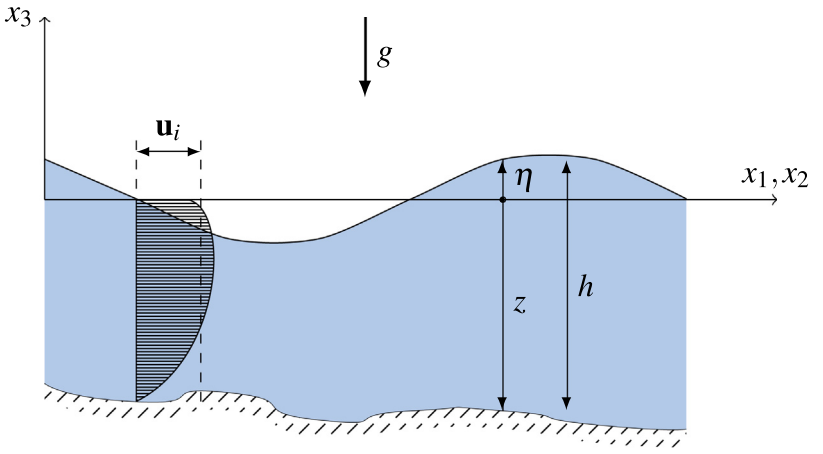

Fig. 1. Diagram and notation for the balance equations (1) and (2).

$$\mathbf{Q} = \begin{Bmatrix} -g(h-z)\dfrac{\partial z}{\partial x_1} + \dfrac{h}{\rho}\dfrac{\partial p_a}{\partial x_1} - \dfrac{1}{\rho}\tau^s_{31} + \dfrac{1}{\rho}\tau^b_{31} \\ -g(h-z)\dfrac{\partial z}{\partial x_2} + \dfrac{h}{\rho}\dfrac{\partial p_a}{\partial x_2} - \dfrac{1}{\rho}\tau^s_{32} + \dfrac{1}{\rho}\tau^b_{32} \\ r \end{Bmatrix} \tag{2d}$$

where $\boldsymbol{\phi}$ is the vector of conserved variables, $\mathbf{F}_i$ is the vector of convective fluxes, $\mathbf{G}_i$ is the vector of viscous fluxes and $\mathbf{Q}$ is the vector source terms. In Fig. 1 there is a representation of the variables and the notation. The coordinates are denoted with the index notation x_i. Since this formulation is defined in a two dimensional space ($n_d = 2$), in the following we will consider $i = 1, 2$. δ_{ij} is the Kronecker delta. The topography is expressed with the variable z and the free surface elevation is expressed in terms of the topography and the total depth, $\eta = z + h$. $\bar{\tau}_{ij}$ are the averaged horizontal stresses, and τ^b_{3i} and τ^s_{3i} denote the bottom and surface friction stresses respectively. Finally, r is the rain source term and p_a is the atmospheric pressure.

The problem is closed with an initial boundary condition,

$$\boldsymbol{\phi}(t = t_0) = \boldsymbol{\phi}_0 \tag{3}$$

where $\boldsymbol{\phi}_0$ are the initial water height and specific discharge.

The following Dirichlet boundary conditions are considered covering all the boundary Γ of the domain Ω:

- Inflow boundary: the flow rate is known

$$\mathbf{q} = \mathbf{q}_{in} \quad \text{in} \quad \Gamma_{in}$$

If the inflow is supercritical, the water depth is also specified

$$\left.\begin{matrix} \mathbf{q} = \mathbf{q}_{in} \\ h = h_{in} \end{matrix}\right\} \quad \text{in} \quad \Gamma_{in}$$

- Outflow boundary: the water depth is known

$$h = h_{out} \quad \text{in} \quad \Gamma_{out}$$

if the outflow is supercritical, no conditions have to be imposed.

- Solid boundary: slip or no slip condition can be imposed

$$\mathbf{q} \cdot \mathbf{n} = 0 \quad \text{or} \quad \mathbf{q} = \mathbf{0} \quad \text{in} \quad \Gamma_{solid}$$

The bottom friction τ^b_{3i} is modelled with the Manning formula generalized for two dimensions as

$$\frac{\tau^b_{3i}}{\rho} = -gn^2\frac{|\mathbf{q}|\mathbf{q}}{h^{7/3}} \tag{4}$$

where n is the Manning coefficient. It defines the resistance to flow by the roughness of the bottom or other macroscopic factors and it is determined empirically. In practice, the Manning coefficient varies from 0.01 for a very smooth bed (concrete) to 0.05 for a rough bed (rocks) [25].

The averaged horizontal stresses are calculated from the combination of the molecular stresses and the Reynolds stresses as follows

$$\frac{\bar{\tau}_{ij}}{\rho} = (\nu + \nu_t)\left(\frac{\partial u_i}{\partial x_j} + \frac{\partial u_j}{\partial x_i} - \frac{2}{3}\delta_{ij}\frac{\partial u_k}{\partial x_k}\right) \tag{5}$$

where ν is the kinematic viscosity and ν_t is the turbulent kinematic viscosity. When any model of turbulence is considered, the turbulent stresses can be included in the bottom friction with the Manning formula [26]. In this work, the turbulent stresses will be neglected.

The balance equation (1) is linearized in the following form

$$\frac{\partial \boldsymbol{\phi}}{\partial t} + \mathbf{A}_i\frac{\partial \boldsymbol{\phi}}{\partial x_i} - \frac{\partial}{\partial x_i}\left(\mathbf{K}_{ij}\frac{\partial \boldsymbol{\phi}}{\partial x_j}\right) + \mathbf{S}\boldsymbol{\phi} + \mathbf{b}_i\frac{\partial z}{\partial x_i} = 0 \tag{6}$$

where the matrices $\mathbf{A}_i$ and $\mathbf{K}_{ij}$ are the linearization matrices of the convective fluxes and the diffusive fluxes respectively. The convective matrices $\mathbf{A}_i$ are obtained after applying the chain rule to the vector of fluxes $\mathbf{F}_i$,

$$\frac{\partial \mathbf{F}_i}{\partial x_i} = \frac{\partial \mathbf{F}_i}{\partial \boldsymbol{\phi}}\frac{\partial \boldsymbol{\phi}}{\partial x_i} \tag{7a}$$

$$\mathbf{A}_i = \frac{\partial \mathbf{F}_i}{\partial \boldsymbol{\phi}} \tag{7b}$$

$$\mathbf{A}_1 = \begin{bmatrix} 2u_1 & 0 & -u_1^2 + c^2 \\ u_2 & u_1 & -u_1u_2 \\ 1 & 0 & 0 \end{bmatrix} \quad , \quad \mathbf{A}_2 = \begin{bmatrix} u_2 & u_1 & -u_1u_2 \\ 0 & 2u_2 & -u_2^2 + c^2 \\ 0 & 1 & 0 \end{bmatrix} \tag{7c}$$

and $c = \sqrt{gh}$ is the wave speed. For the one dimensional case, the eigenvalues of $\mathbf{A}$ are $\lambda_{1,2} = u \pm c$. In two dimensions, given the unit vector $\mathbf{e}$, the eigenvalues of the matrix $e_i\mathbf{A}_i$ are $\lambda_{1,3} = \mathbf{e}\cdot\mathbf{u} \pm c$ and $\lambda_2 = \mathbf{e}\cdot\mathbf{u}$. The eigenvalues are real and always different ($\lambda_1 < \lambda_2 < \lambda_3$), this property is called strictly hyperbolicity [27]. The eigenvalues are velocities, namely the ones of surface waves on the fluid. Note that in the dry zones, where $h = 0$, the eigenvalues coincide and the system is no longer hyperbolic. This introduces difficulties at theoretical and numerical level.

The viscous fluxes $\mathbf{G}_i$ are rewritten in a more convenient manner as $\mathbf{G}_i = \mathbf{K}_{ij}\partial\boldsymbol{\phi}/\partial x_j$. The fourth order tensor $\mathbf{K}_{ij}$ is obtained making use of Eq. (5). It is an auxiliary variable to write the linearized tensor in Voigt's notation and it is explained in more detail in Section 4.

The vectors $\mathbf{b}_i$ are the result of the linearization of the topography. They are obtained by the linearization of the fluxes $\mathbf{F}_i$ respect to the topography coordinate z. Rearranging terms with the independent vector $\mathbf{Q}$ yields

$$\mathbf{b}_i = \begin{bmatrix} \delta_{i1}c^2 \\ \delta_{i2}c^2 \\ 0 \end{bmatrix} \tag{8}$$

The bottom friction term acting on the source term vector is linearized using a reaction matrix $\mathbf{S}$

$$\mathbf{S} = \begin{bmatrix} \frac{gn^2|\mathbf{u}|}{h^{4/3}} & 0 & 0 \\ 0 & \frac{gn^2|\mathbf{u}|}{h^{4/3}} & 0 \\ 0 & 0 & 0 \end{bmatrix} \tag{9}$$

In the following sections, the rain, the atmospheric pressure and the wind friction will be neglected.

3. FIC stabilization

We will consider the quasi-linear balance equations written in residual form as a vector

$$\mathbf{r} := \frac{\partial \boldsymbol{\phi}}{\partial t} + \mathbf{A}_i\frac{\partial \boldsymbol{\phi}}{\partial x_i} - \frac{\partial}{\partial x_i}\left(\mathbf{K}_{ij}\frac{\partial \boldsymbol{\phi}}{\partial x_j}\right) + \mathbf{S}\boldsymbol{\phi} + \mathbf{b}_i\frac{\partial z}{\partial x_i} \qquad i,k \in \{1, n_d\} \tag{10}$$

where $n_d = 2$ is the number of dimensions. The size of the vector $\mathbf{r}$ is equal to the number of balance equations, $n_b = 3$.

In the one dimensional case ($n_d = 1$) and scalar balance ($n_b = 1$), the FIC-based stabilization is based on a modified non local version of the governing equations as [13]

$$r - \frac{1}{2} l^e \frac{\partial r}{\partial x} = 0 \tag{11}$$

The stabilization parameter l^e is usually taken the element length. However, in 2D and 3D, or when the number of balance equations n_b is different than n_d, the choice of the l^e parameter is non trivial. Several approaches can be found in the literature. In [13] l^e is chosen as a vector, but in later publications such as [14] a generalized formulation for different values of n_d and n_b was presented. For the stabilization of the Navier–Stokes equations different projections of the element size over the velocity and over the velocity gradient have been proposed [18]. Here we will use index notation for the residual vector $\mathbf{r}$ in order to distinguish the indices that goes to n_d or to n_b. To sum up, the different forms of the FIC stabilization procedure can be written as

$$r_k - \frac{1}{2} l_i^e \frac{\partial r_k}{\partial x_i} = 0 \qquad i \in \{1, n_d\}\ ,\ k \in \{1, n_b\} \tag{12a}$$

$$r_k - \frac{1}{2} l_u^e \frac{u_i}{\|\mathbf{u}\|} \frac{\partial r_k}{\partial x_i} = 0 \qquad i, k \in \{1, n_d\} \tag{12b}$$

$$r_k - \frac{1}{2} l_{g_i}^e \frac{\partial \mathbf{u}/\partial x_i}{\|\nabla u_i\|} \frac{\partial r_k}{\partial x_i} = 0 \qquad i, k \in \{1, n_d\} \tag{12c}$$

In this paper we propose a stabilization term which is oriented along the characteristics of the hyperbolic equations, as

$$r_k - \frac{1}{2} l^e \frac{\mathbf{A}_i}{\lambda} \frac{\partial r_k}{\partial x_i} = 0 \qquad i \in \{1, n_d\}\ ,\ k \in \{1, n_b\} \tag{13}$$

For consistency the linearization matrix $\mathbf{A}_i$ is normalized with the maximum eigenvalue $\lambda = |\mathbf{u}| + c$. This stabilization is analogue to the virtual multi-scale stabilization proposed in [28]. The linearization matrix $\mathbf{A}_i$ provides a weighting procedure between the stabilization of the convective and the mixed wave equation terms. In practice the element size is multiplied by an algorithmic constant in order to control the amount of diffusion added by the stabilization and it will be studied in the examples of Section 5. Recovering the vector notation for the residual, the FIC-balance reads

$$\mathbf{r} - \beta l^e \frac{\mathbf{A}_i}{\lambda} \frac{\partial \mathbf{r}}{\partial x_i} \qquad i \in \{1, n_d\} \tag{14}$$

The FIC formulation is the result of introducing the residual of the shallow water equations (10) into the expression in Eq. (14). The variational expression of the equation is obtained by multiplying the equation by a test function ω_k and integrating over the domain Ω. This gives

$$\int_\Omega \left(\omega_k \mathbf{r} - \omega_k \beta l^e \frac{\mathbf{A}_i}{\lambda} \frac{\partial \mathbf{r}}{\partial x_i} \right) d\Omega = 0 \tag{15}$$

The second term of Eq. (15) is integrated by parts. Note that the element length l^e, the linearization matrix $\mathbf{A}_i$ and its eigenvalue λ are defined constant inside the element. Hence, the boundary integral which appears after integration by parts should be understood as the boundary of all the elements

$$\int_\Omega \omega_k \mathbf{r} d\Omega + \int_\Omega \beta l^e \frac{\mathbf{A}_i}{\lambda} \frac{\partial \omega_k}{\partial x_i} \mathbf{r} d\Omega - \sum_e \int_{\Gamma_e} \beta l^e \frac{\mathbf{A}_i}{\lambda} \omega_k n_k \mathbf{r} d\Gamma = 0 \tag{16}$$

In this work we neglect the boundary integrals assuming that the residual $\mathbf{r}$ is null at the boundary of the elements. At this point we introduce the balance equation (10) and integrate by parts the diffusive term. Derivatives of order

higher tan two will be neglected since we are using linear triangles (see Section 4). The result is

$$\int_\Omega \left(\omega_k \frac{\partial \boldsymbol{\phi}}{\partial t} + \omega_k \mathbf{A}_i \frac{\partial \boldsymbol{\phi}}{\partial x_i} + \frac{\partial \omega_k}{\partial x_i} \mathbf{K}_{ij} \frac{\partial \boldsymbol{\phi}}{\partial x_j} + \omega_k \mathbf{S}\boldsymbol{\phi} + \omega_k \mathbf{b}_i \frac{\partial z}{\partial x_i} \right) d\Omega$$

$$+ \int_\Omega \frac{\beta l^e}{\lambda} \left(\frac{\partial \omega_k}{\partial x_j} \mathbf{A}_j \frac{\partial \boldsymbol{\phi}}{\partial t} + \frac{\partial \omega_k}{\partial x_j} \mathbf{A}_j \mathbf{A}_i \frac{\partial \boldsymbol{\phi}}{\partial x_i} + \frac{\partial^2 \omega_k}{\partial x_j^2} \mathbf{A}_j \mathbf{K}_{ij} \frac{\partial \boldsymbol{\phi}}{\partial x_i} \right.$$

$$\left. + \frac{\partial \omega_k}{\partial x_j} \mathbf{A}_j \left(\mathbf{S}\boldsymbol{\phi} + \mathbf{b}_i \frac{\partial z}{\partial x_i} \right) \right) d\Omega = 0 \tag{17}$$

Eq. (17) is the stabilized variational form for the shallow water equations, similar to the expression obtained by SUPG. Note that the parameter $\beta l^e/\lambda$ is analogous to the characteristic time τ of the classical SUPG or GLS techniques [18].

3.1. Shock capturing stabilization

In this section we explore other possibilities of the characteristic length definition in order to obtain a shock capturing stabilization. Here, the mass balance and the momentum balance are considered separately and the characteristic length is projected onto the gradient of the unknown

$$\text{Momentum balance:} \quad r_i^q - \frac{l^e}{2\,\|\nabla q_i\|} \frac{\partial q_i}{\partial x_j} \frac{\partial r_i^q}{\partial x_j} = 0 \tag{18a}$$

$$\text{Mass balance:} \quad r^h - \frac{l^e}{2\,\|\nabla h\|} \frac{\partial h}{\partial x_j} \frac{\partial r^h}{\partial x_j} = 0 \tag{18b}$$

Multiplying the momentum balance equation (18a) by a proper test function ω_k, integrating over the domain in the same way as in Eq. (15), one obtains the following variational form:

$$\int_\Omega \omega_k r_i^q d\Omega - \int_\Omega \omega_k \frac{l^e}{2\,\|\nabla q_i\|} \frac{\partial q_i}{\partial x_j} \frac{\partial r_i^q}{\partial x_j} d\Omega = 0 \tag{19}$$

After integration of Eq. (19) by parts and rearranging terms we obtain

$$\int_\Omega \omega_k r_i^q d\Omega + \int_\Omega \frac{\partial \omega_k}{\partial x_j} \frac{l^e r_i^q}{2\,\|\nabla q_i\|} \frac{\partial q_i}{\partial x_j} d\Omega$$

$$+ \int_\Omega \omega_k \frac{\partial}{\partial x_j} \left(\frac{l^e}{2\,\|\nabla q_i\|} \frac{\partial q_i}{\partial x_j} \right) r_i^q d\Omega - \int_\Omega \frac{\partial}{\partial x_j} \left(\omega_k \frac{l^e}{2\,\|\nabla q_i\|} \frac{\partial q_i}{\partial x_j} r_i^q \right) d\Omega = 0 \tag{20}$$

Since we will use linear triangles (see Section 4), the last two terms of Eq. (20) are dropped because they involve derivatives of the characteristic length and can be transformed into a boundary integral.

The same procedure is applied to the mass balance equation (18b). As a result we obtain the following system of equations for both unknowns

$$\text{Momentum balance:} \quad \int_\Omega \omega_k r_i^q d\Omega + \int_\Omega \frac{\partial \omega_k}{\partial x_j} \frac{l^e r_i^q}{2\,\|\nabla q_i\|} \frac{\partial q_i}{\partial x_j} d\Omega = 0 \tag{21a}$$

$$\text{Mass balance:} \quad \int_\Omega \omega_k r^h d\Omega + \int_\Omega \frac{\partial \omega_k}{\partial x_j} \frac{l^e r^h}{2\,\|\nabla h_i\|} \frac{\partial q_i}{\partial x_j} d\Omega = 0 \tag{21b}$$

The above expressions (21) are equivalent to a classical shock capturing method, in which the artificial diffusivity k_{art} and artificial viscosity ν_{art} can be identified as

$$\nu_{art} = \frac{1}{2} \alpha l_e \frac{|r_i^q|}{\|\nabla u_i\|} \tag{22a}$$

$$k_{art} = \frac{1}{2} \alpha l_e \frac{|r^h|}{\|\nabla h\|} \tag{22b}$$

where α is an algorithmic constant.

Such approach can be refined by introducing the stabilization along the streamlines. This way, k_{art} and ν_{art} need to be added only in the crosswind direction. The diffusive term is added to the mass balance with the following orthogonal tensor

$$\mathbf{D}_{art} = k_{art}\left(\mathbf{I} - \frac{1}{|\mathbf{u}|^2}\mathbf{u}\otimes\mathbf{u}\right) \tag{23}$$

The viscosity is introduced into the momentum balance with a fourth order tensor in the crosswind direction. Using Voigt's notation,

$$\mathbf{C}_{art} = \nu_{art}\mathbf{I}_4\mathbf{J} \tag{24}$$

with

$$\mathbf{J} = \begin{bmatrix} 1-\frac{q_1 q_1}{\mathbf{qq}} & -\frac{q_1 q_2}{\mathbf{qq}} & 0 \\ -\frac{q_1 q_2}{\mathbf{qq}} & 1-\frac{q_2 q_2}{\mathbf{qq}} & 0 \\ 0 & 0 & 1-\frac{q_1 q_2}{\mathbf{qq}} \end{bmatrix} \tag{25}$$

where $\mathbf{I}_4$ is the fourth order identity tensor for the stresses, which is derived from Eq. (5) and will be defined in Section 4.

4. Finite element formulation

It is conventional to use higher order of interpolation for the momentum or velocity than for the water depth or free surface in order to develop stable finite element formulations [4,20,29]. In this work we restrict ourselves to linear triangles for both $\mathbf{q}$ and h unknowns, since the FIC-FEM procedure is intrinsically stable. For that reason, all terms including spatial derivatives of order higher than two will be neglected. Bilinear quadrilaterals and higher order elements with the same number of degrees of freedom for all the variables will be also stable.

4.1. Spatial discretization

A finite element discretization Ω_h is introduced in the domain Ω and the problem variables can be interpolated with the basis functions of the finite elements space as

$$\phi_i = \sum_{a}^{n_\Omega} N_a(\mathbf{x})\phi_{ai} \qquad i \in \{1, n_b\} \tag{26}$$

where n_Ω represents the total number of nodes in Ω_h and ϕ_i are the problem variables defined in (2). Note that the shape functions are the same for all the variables, h and q_i. Here we introduce the notation $\boldsymbol{\phi}_h$ for the vectors of nodal unknowns -momentum and water height- on the finite element domain. Following the standard Galerkin discretization, the shape functions N_a are used to interpolate the test functions ω_k and the unknowns. The continuous Eq. (17) is combined with Eq. (21) and can be expressed as the following algebraic system of equations

$$[\mathbf{M}+\mathbf{M}_F]\dot{\boldsymbol{\phi}}_h + [\mathbf{G}+\mathbf{G}_F+\mathbf{L}+\mathbf{L}_{SC}+\mathbf{R}+\mathbf{R}_F]\boldsymbol{\phi}_h = \mathbf{T}+\mathbf{T}_F \tag{27}$$

where the dot ($\dot{}$) means temporal derivative. The matrices in Eq. (27) without subscript are related to the original problem (10); the matrices with subscript F correspond to the terms added by the FIC procedure to ensure stability, and those with the subscript SC are the terms added by the shock capturing technique. Using a, b to denote the nodes, i, j to denote the space dimension index and k, l to denote the balance equation number, the matrices in Eq. (27) are defined as

$$\mathbf{M}^{ab} = \int_{\Omega_e} N_a \mathbf{I} N_b d\Omega \qquad \mathbf{G}^{ab} = \int_{\Omega_e} N_a \mathbf{A}_i \frac{\partial N_b}{\partial x_i} d\Omega$$

$$\mathbf{L}^{ab} = \int_{\Omega_e} \mathbf{B}_a \begin{bmatrix} \mathbf{C} & \mathbf{0} \\ \mathbf{0} & \mathbf{D} \end{bmatrix} \mathbf{B}_b^T d\Omega \qquad \mathbf{R}^{ab} = \int_{\Omega_e} N_a \mathbf{S} N_b d\Omega \tag{28}$$

$$\mathbf{T}^{ab} = \int_{\Omega_e} N_a \mathbf{b}_i \frac{\partial z}{\partial x_i} d\Omega + \int_{\Gamma_e} N_a \mathbf{t}_b d\Gamma$$

where the diffusive matrix $\mathbf{L}^{ab}$ is defined using the derivatives matrix $\mathbf{B}_a$ and the isotropic tensors $\mathbf{C}$ and $\mathbf{D}$ of viscosity and diffusivity. Note that the diffusivity is zero, but the matrix structure will be reused for the stabilization. The viscosity tensor in Voigt's notation is constructed using the linearization matrices $\mathbf{K}_{ij}$. The matrix and the tensors are given by

$$\mathbf{B}_a = \begin{bmatrix} \frac{\partial N_a}{\partial x_1} & 0 & \frac{\partial N_a}{\partial x_2} & 0 & 0 \\ 0 & \frac{\partial N_a}{\partial x_2} & \frac{\partial N_a}{\partial x_1} & 0 & 0 \\ 0 & 0 & 0 & \frac{\partial N_a}{\partial x_1} & \frac{\partial N_a}{\partial x_2} \end{bmatrix} \tag{29a}$$

$$\mathbf{C} = \nu \mathbf{I}_4 \ , \quad \mathbf{D} = k\mathbf{I}_2 \ , \quad \mathbf{I}_4 = \frac{1}{3}\begin{bmatrix} 2 & -1 & 0 \\ -1 & 2 & 0 \\ 0 & 0 & 3 \end{bmatrix} \ , \quad \mathbf{I}_2 = \begin{bmatrix} 1 & 0 \\ 0 & 1 \end{bmatrix} \tag{29b}$$

The stabilization and shock capturing terms from Eq. (27) result in analogous matrices with higher derivatives order, the boundary integral is neglected, i.e.,

$$\begin{aligned} \mathbf{M}_F^{ab} &= \int_{\Omega_e} \frac{\beta l^e}{2} \frac{\partial N_a}{\partial x_i} \mathbf{A}_i N_b d\Omega & \mathbf{G}_F^{ab} &= \int_{\Omega_e} \frac{\beta l^e}{2} \frac{\partial N_a}{\partial x_i} \mathbf{A}_i \mathbf{A}_j \frac{\partial N_b}{\partial x_j} d\Omega \\ \mathbf{L}_{SC}^{ab} &= \int_{\Omega_e} \mathbf{B}_a \begin{bmatrix} \mathbf{C}_{\text{art}} & \mathbf{0} \\ \mathbf{0} & \mathbf{D}_{\text{art}} \end{bmatrix} \mathbf{B}_b^T d\Omega & \mathbf{R}_F^{ab} &= \int_{\Omega_e} \frac{\beta l^e}{2} \frac{\partial N_a}{\partial x_i} \mathbf{A}_i \mathbf{S} N_b d\Omega \\ \mathbf{T}_F^{ab} &= \int_{\Omega_e} \frac{\beta l^e}{2} \frac{\partial N_a}{\partial x_i} \mathbf{A}_i \mathbf{b}_j \frac{\partial z}{\partial x_j} d\Omega \end{aligned} \tag{30}$$

4.2. Temporal integration

The resulting expression from the spatial discretization (27) can be written in the following compact form

$$\tilde{\mathbf{M}}\dot{\boldsymbol{\phi}}_h + \tilde{\mathbf{K}}\boldsymbol{\phi}_h = \tilde{\mathbf{f}} \tag{31}$$

where the symbol ($\tilde{}$) denotes the assembly of the system matrices and vectors for all the elements. We have integrated this equation introducing a time discretization using the well known BDF2 implicit scheme [30,31]. The system of equations in a discrete time domain yields

$$\begin{aligned} \tilde{\mathbf{M}}\dot{\boldsymbol{\phi}}_h^{n+1} + \tilde{\mathbf{K}}^{n+1}\boldsymbol{\phi}_h^{n+1} &= \tilde{\mathbf{f}}^{n+1} \\ \dot{\boldsymbol{\phi}}_h^{n+1} &= \beta_0\boldsymbol{\phi}_h^{n+1} + \beta_1\boldsymbol{\phi}_h^{n} + \beta_2\boldsymbol{\phi}_h^{n-1} \end{aligned} \tag{32}$$

We will consider a variable time step to compute the BDF coefficients using the notation $t^{n+1} = t^n + \Delta t^n$:

$$\begin{aligned} \beta_0 &= \tau(\rho^2 + 2\rho) \\ \beta_1 &= -\tau(\rho^2 + 2\rho + 1) \\ \beta_2 &= \tau \end{aligned} \tag{33}$$

with

$$\begin{aligned} \tau &= \frac{1}{\Delta t^n(\rho^2 + \rho)} \\ \rho &= \frac{\Delta t^{n-1}}{\Delta t^n} \end{aligned} \tag{34}$$

The solution of this implicit system requires an iterative procedure. We have used the Newton–Raphson method, by which the problem unknowns are computed in an incremental way as $\boldsymbol{\phi}_h^{n+1,i+1} = \boldsymbol{\phi}_h^{n+1,i} + \delta\boldsymbol{\phi}_h^i$, where the superscript i denotes the non linear iteration. This notation allows us to rewrite the system of Eqs. (32) defining a left hand side matrix multiplied by the increment $\delta\boldsymbol{\phi}_h^i$ and a right hand side vector which depends on the previous non linear iteration as

$$[\beta_0\tilde{\mathbf{M}} + \tilde{\mathbf{K}}^{n+1,i}]\delta\boldsymbol{\phi}_h^i = \tilde{\mathbf{f}}^{n+1,i} - \tilde{\mathbf{K}}^{n+1,i}\boldsymbol{\phi}_h^{n+1,i} - \tilde{\mathbf{M}}\dot{\boldsymbol{\phi}}_h^{n+1,i} \tag{35}$$

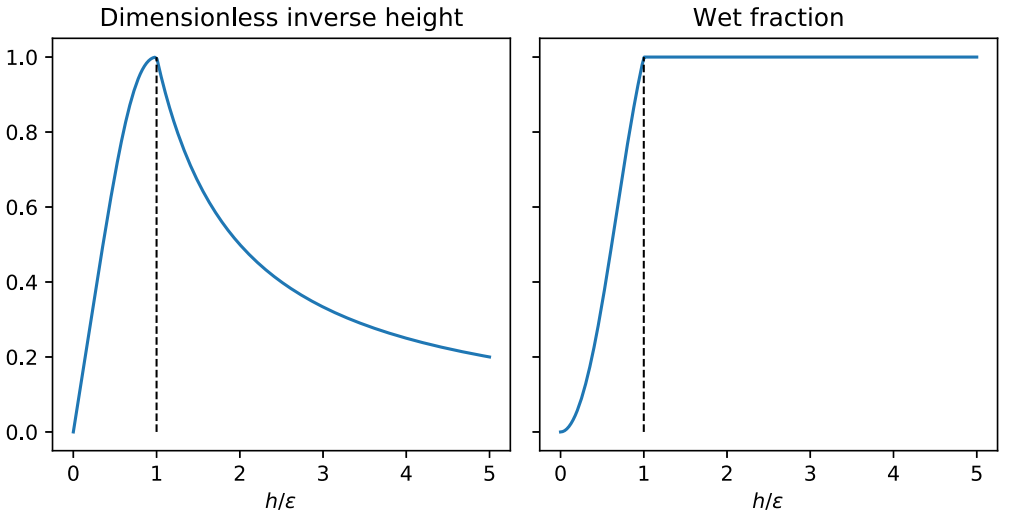

Fig. 2. Dimensionless functions to compute the inverse height and the wet fraction.

The first non linear iteration $\boldsymbol{\phi}_h^{n+1,0}$ is initialized using a prediction given from the BDF formula at the last time step:

$$\boldsymbol{\phi}_h^{n+1,0} = \boldsymbol{\phi}_h^n + \Delta t^n \dot{\boldsymbol{\phi}}_h^n \tag{36}$$

4.3. Dry domain model

When small or quasi zero water depths are involved in simulations, some instabilities may arise. In addition, the solution of the time integration scheme requires the inverse of a matrix which is singular in the dry regions. In this section we review the challenges associated to such a problem, and the way we have circumvented them.

Recovery of the velocity field. The evaluation of the characteristic matrices $\mathbf{A}_i$ involves the velocities, which are recovered given the primary variables $\boldsymbol{\phi}$ from the previous iteration. Since the computation of the velocity is the result of dividing the discharge by the water height, this operation is ill-conditioned in the dry regions. In this research, the velocity field is computed in a two step procedure. First of all, the inverse of the water depth is computed at each element following the next expression, initially proposed in [32]:

$$\hat{h}^{-1} := \frac{\sqrt{2}\max(h,0)}{\sqrt{h^4 + \max(h^4, \varepsilon^4)}} \tag{37}$$

where ε is a threshold which depends on the element size; usually $\varepsilon = 0.1 l_e$ is chosen. Fig. 2 shows a dimensionless representation of Eq. (37). The second step in the velocity computation is a diffusive projection on the nodes:

$$\mathbf{M}_L \mathbf{u} = \hat{h}_k^{-1} \mathbf{M}(\mathbf{q}) \tag{38}$$

where $\mathbf{M}$ is the consistent mass matrix and $\mathbf{M}_L$ is the lumped mass matrix. This projection will introduce some artificial diffusion in the velocity field near the dry-wet interface reducing the possible maxima extrema.

The expression(37) tends to zero in dry or partially dry regions, while the analytical expression of the height inverse is recovered when $h > \varepsilon$.

Partially wet elements. At the elements where the shoreline is located, the interpolated water depth will not represent the real water surface. Therefore, those elements need a special consideration in order to prevent unrealistic oscillations. Excluding those elements from the computations is equivalent to introduce an artificial barrier, and the inclusion of those elements will incur in a consideration of an extra volume of water. We chose to include all the elements in the computation and to modify the balance equations in order to satisfy equilibrium at rest (Fig. 3).

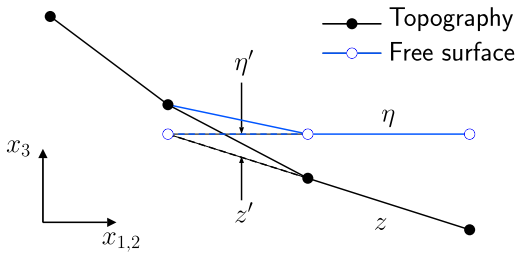

Fig. 3. Dry, wet and partially wet elements in 1D. The dashed line shows the modified topography and the corresponding free surface.

This is achieved by introducing a modified topography z' which is obtained imposing the following equilibrium condition:

$$\frac{\partial \eta'}{\partial x_i} = \frac{\partial z'}{\partial x_i} + \frac{\partial h}{\partial x_i} = \mathbf{0} \tag{39}$$

Following the idea of [23], the identification of partially wet elements is done across the definition of a wet fraction function. In this research, instead of modifying the vertical integration of the Navier–Stokes equations, the wet fraction is defined making use of the pseudo inverse $\hat{h}^{-1}$. The wet fraction w reads:

$$w = h\hat{h}^{-1} \tag{40}$$

The wet fraction function is defined in all the elements -wet, dry and partially dry- and its value goes from 0 for dry elements to 1 for wet elements (see Fig. 2) This function makes possible to construct the source system vector $\mathbf{T}$ (see Eqs. (27) and (28)) with a linear combination between the two topographies as $wz + (1 - w)z'$.

Avoiding the singularity of the system matrix. Since all the elements are included in the computational domain, the last issue to overcome with small water depths are the numerical difficulties stated in Section 2. When there is a null water depth, the theoretical flow rate and velocity are zero. In that point the matrices $\mathbf{A}_i$ are not invertible and the eigenvalues are all equal to zero. In that case, the hyperbolicity property of the system is lost. In practice, due to spurious oscillations, the flow rate and the velocity may be different from zero. The idea is to freeze the flow and to allow to invert the system matrix adding a diagonal of non zero terms to the momentum equation, i.e.,

$$\mathbf{G} := \mathbf{G} + \xi \,\mathrm{diag}(1, 1, 0) \tag{41}$$

The selection of the areas where there is a dry domain is controlled with the wet fraction function and ξ is defined as

$$\xi = k(1 - w) \tag{42}$$

In our numerical experiments we have chosen $k = 10^3$. The addition of a diagonal matrix remembers the artificial Manning friction proposed in [20]. This term plays the role of freezing the flow in dry areas.

Mass conservation properties. The stabilized method proposed is not monotonic and the dry domain model is acting to ensure stability, but it does not provide monotonicity. We note that all the modifications have been done at the momentum balance level. This means that mass is conserved globally by the weak formulation, but the mass sign preservation is not guaranteed.

Both unknowns, water depth and flow rate, are continuous at the dry-wet interface, but its derivatives are discontinuous. Even though the shock capturing scheme can not avoid this kind of oscillations, it will mitigate them, and the order of accuracy will be lost due to the introduction of the non-linear artificial diffusion [33].

5. Examples

The FIC-FEM formulation presented has been implemented in KratosMultiphysics [34,35], an open source framework of numerical methods written in C++. In this section we present four different examples. Three of them are oriented to verify a single aspect of the procedure explained in this research, the global stabilization, the shock capturing technique and the dry-wet interface. The last one is devoted to test all the capabilities of the formulation in a practical case for which experimental data is available.

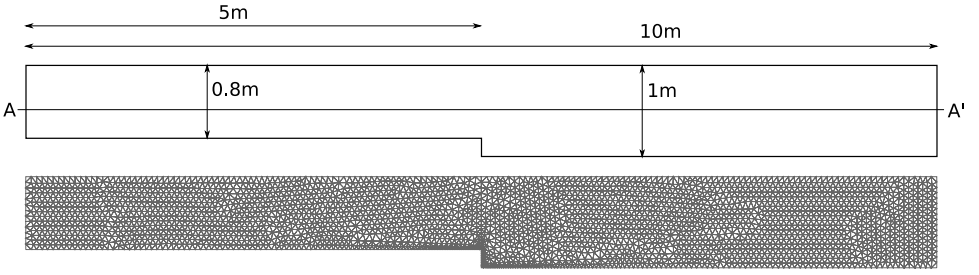

Fig. 4. Channel with a backward step. Domain and mesh used in the simulation. All the boundary conditions are slip. The average element size is 0.06 m. Near the obstacle the mesh size is 0.02 m. There are 3.125 nodes and 5.826 elements.

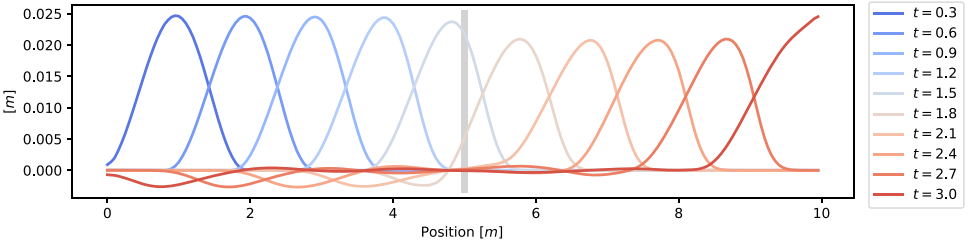

(a) Time from 0 to 3s

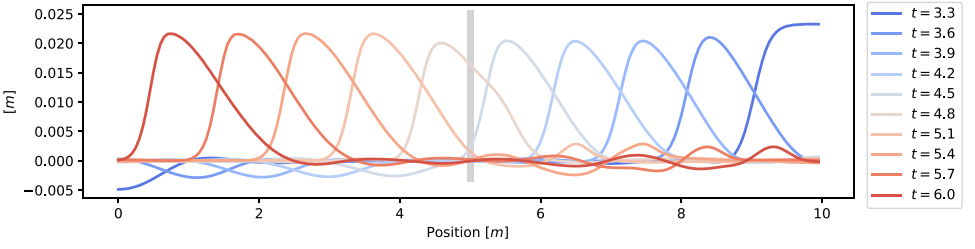

(b) Time from 3 to 6s

Fig. 5. Channel with a backward step. Timestamps of the free surface along the cut AA' from Fig. 4. (a) The initial perturbation is propagating to the right. (b) Propagation of the reflected wave from right to left.

5.1. Wave in a channel with a backward step

The aim of the first example is to show that the Galerkin formulation applied to the shallow water equations is unstable and how the present stabilization method can overcome this issue. A calibration of the stabilization parameter is performed to optimize the effect of the stabilization terms in the obtained solution. We study the propagation of a wave in a channel with a backward step (Fig. 4) where all the boundaries are slip. The channel depth is 1 m. An initial perturbation in the free surface at the left wall generates a wave which travels from 0 to 6s. The initial perturbation reads

$$\eta(t=0) = 0.05\cos(\pi x) \quad \text{if} \quad x < 1, \quad \eta = 0 \quad \text{otherwise} \tag{43}$$

The wave is reflected at the right wall and then faces the step in the opposite direction. Fig. 5 shows the propagation of the wave along the channel. The problem is discretized with a mesh fine enough to test the artificial diffusion added by the stabilization (Fig. 4). The average element size is 0.06 m and near the corner the mesh is refined to 0.02 m. The time step is set automatically to keep a maximum Courant number equal to 1.0 at every step. The problem is run three times with different algorithmic constants $\beta = 0.001$, 0.01 and 0.1. In this example, the shock capturing term is disabled.

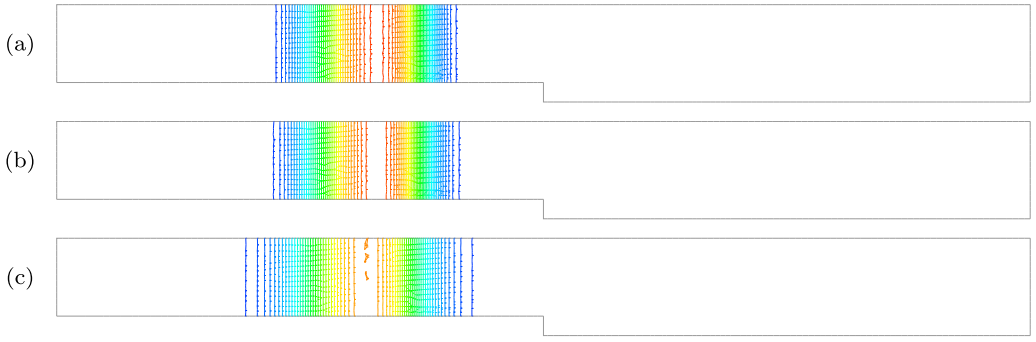

Fig. 6. Channel with a backward step. Contour plots of the free surface elevation at time $t = 1$ s for different stabilization factors. (a) $\beta = 0.001$, (b) $\beta = 0.01$, (c) $\beta = 0.1$.

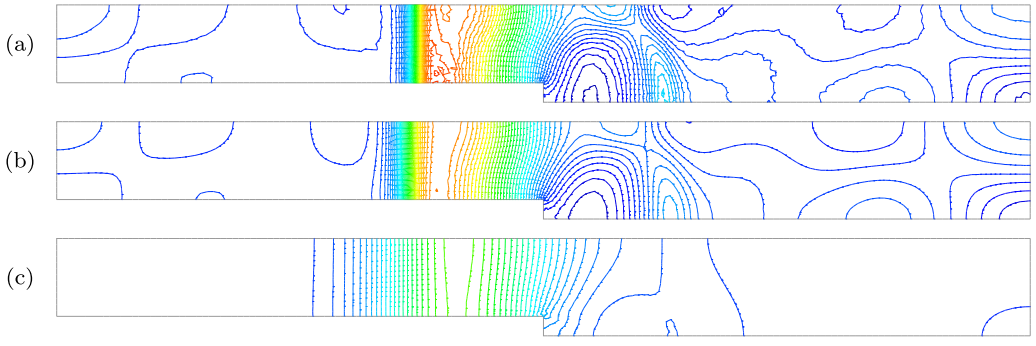

Fig. 7. Channel with a backward step. Contour plots of the free surface elevation at time $t = 5$ s for different stabilization factors. (a) $\beta = 0.001$, (b) $\beta = 0.01$, (c) $\beta = 0.1$.

The best results are achieved with the intermediate value and it has been fixed for the rest of the examples in this paper. Figs. 6 and 7 show that the lower value of β is not enough to provide stability, while the higher value is over diffusive.

5.2. Oscillation in a parabolic basin

The second example is a classical benchmark oriented to test the accuracy of the location of the moving boundary. The topography follows a parabolic profile while the initial free surface elevation is planar and intersects the topography. The initial configuration corresponds to zero velocity but the free surface is in a non horizontal plane. The solution of the problem is oscillatory and the free surface elevation remains planar. An analytical solution can be found in the compilation made by Delestre et al. [36].

The domain Ω is defined in the interval $[0, L] \times [0, 1]$ m where $L = 10$ m and all the boundaries are reflective ($\mathbf{u} \cdot \mathbf{n} = 0$). The topography is given by the following expression

$$z(x, y) = h_0 \left(\frac{1}{a^2} \left(x - \frac{L}{2} \right)^2 - 1 \right) \tag{44}$$

The primitive variables are defined by

$$h(x, y) = \begin{cases} -h_0 \left(\left(\frac{1}{a} \left(x - \frac{L}{2} \right) + \frac{1}{2a} \cos(2Bt) \right)^2 - 1 \right) & \text{if } x_1(t) < x < x_2(t) \\ 0 & \text{otherwise} \end{cases} \tag{45a}$$

$$\mathbf{u}(x, y) = \begin{cases} (B, 0) \sin(2Bt) & \text{if } x_1(t) < x < x_2(t) \\ (0, 0) & \text{otherwise} \end{cases} \tag{45b}$$

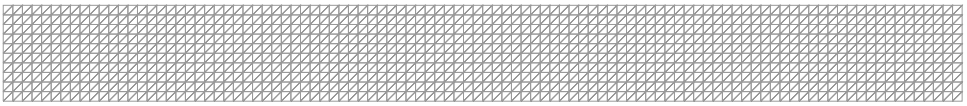

Fig. 8. Parabolic basin. One of the meshes used in the analysis. The element size is 0.1 m.

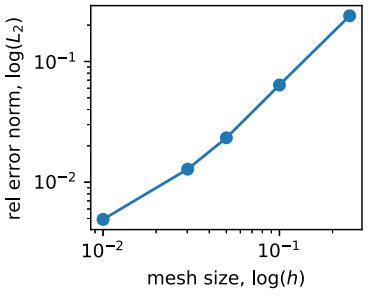

n_{nodes}	Δx	Δt	CFL	$L_2(e_{rel})$
205	0.25	0.008	0.5	0.24
1,111	0.1	0.003	0.5	0.064
4,221	0.05	0.002	0.5	0.023
11,356	0.03	0.001	0.5	0.013
101,101	0.01	0.0003	0.5	0.0049

Fig. 9. Parabolic basin. Convergence analysis for the water height.

where $B = \sqrt{2gh_0}/2a$, and x_1, x_2 are time dependent functions which define the location of the dry-wet interface:

$$x_1(t) = -\frac{1}{2}\cos(2Bt) - a + \frac{L}{2}$$
$$x_2(t) = -\frac{1}{2}\cos(2Bt) + a + \frac{L}{2} \tag{46}$$

In that example the selected parameters are $h_0 = 1$ m and $a = 1$ m.

The domain Ω is discretized using several meshes in order to perform a convergence analysis. The meshes employed are listed in Fig. 9. Fig. 8 shows one of the intermediate mesh. Once the simulation begins, the water starts to oscillate on the parabolic basin and the velocity field is constant on the spatial domain, while follows a periodic function respect to the time.

Fig. 10 shows a cut along the mesh at different times. The most challenging problem is to capture the discontinuity of the velocity. Even though the velocity presents a discontinuity, it isn't the origin of the oscillatory behavior since the velocity is not a degree of freedom. It can be appreciated how the discontinuity of the velocity is not an issue.

A mass conservation test is performed with the mesh of size 0.05 m in a simulation of 5 s. The results are presented in Fig. 11. The integration of the mass is performed over all the domain and over the wet domain. The wet domain is identified with the wet fraction, requiring that it is equal to 1. Since the presented scheme is not mass sign preserving, the wet mass can not be equal to the total mass and a small fraction is lost from the wet domain. The loss depends on the element size and presents an oscillatory behavior inherent of the method. Fig. 11 shows that the mass loss is bounded and the mean does not increase with time.

Fig. 12 shows the results using the finest mesh. The discretization is not shown for the sake of simplicity. As expected, there is no variation on the results in the transversal section.

5.3. Short channel with smooth transition and shock

The third example in a benchmark based on the Mac Donald's type solutions [37]. The analytical solution can be found in the same compilation than the previous example [36]. This test presents a channel with a steady state solution. There is a subcritical inlet and a transcritical flow is produced. The outlet is also subcritical and then a shock is generated at 2/3 of the channel. The aim of this example is to evaluate the shock capturing technique presented and the correct location of the hydraulic jump, which depends on the bottom friction law.

Here we will consider the 1D shallow water equations without diffusion and only with Manning bottom friction as source term. A steady state solution satisfies $\frac{\partial q}{\partial x} = 0$ and Eq. (1) reduces to

$$\frac{\partial z}{\partial x} = \left(\frac{v^2}{gh} - 1\right)\frac{\partial h}{\partial x} - n^2\frac{|v|v}{h^{4/3}} \tag{47}$$

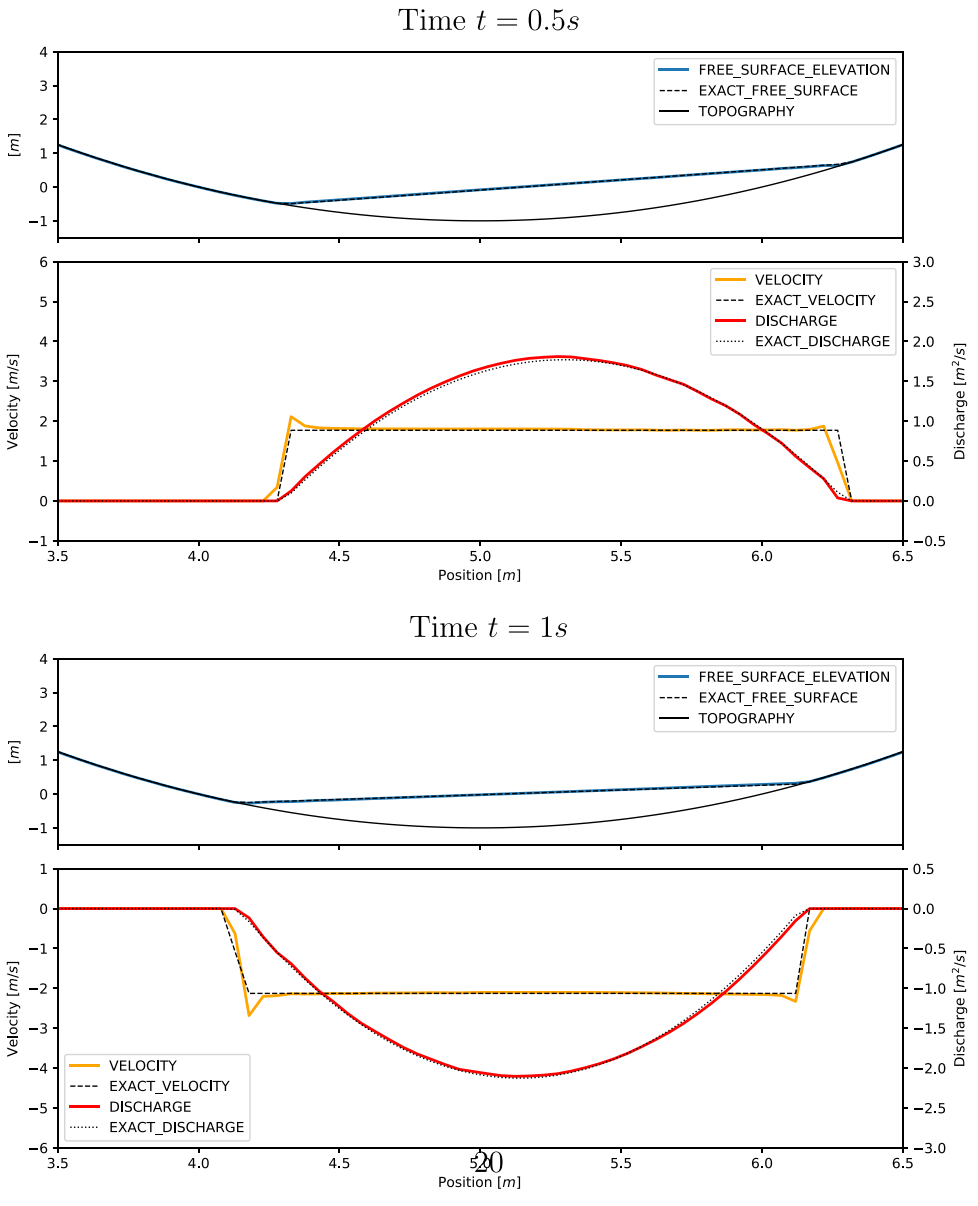

Fig. 10. Parabolic basin. Cuts along the mesh of size 0.03 m at different times. There are 333 nodes on the cut.

This relation allows to integrate the topography given an analytical expression for the water height. Another approach in hydraulics is to consider a given discharge and topography and integrate the water height using Eq. (47). Following both approaches exact solutions can be obtained. Since this expression involves the bottom friction, we can verify if the friction term is correctly coded in order to satisfy the steady state.

For this benchmark we have considered the domain defined by the spatial domain $[0, 100] \times [0, 5]$ which is a channel of 100 m length and 5 m width (Fig. 13), and the following boundary conditions:

$$\begin{aligned} q_x &= 2 \text{ m/s} \quad \text{in} \quad \Gamma_{upstream} \\ h &= h_{ex}(100) \quad \text{in} \quad \Gamma_{downstream} \\ q_y &= 0 \quad \text{in} \quad \Gamma_{walls} \end{aligned} \tag{48}$$

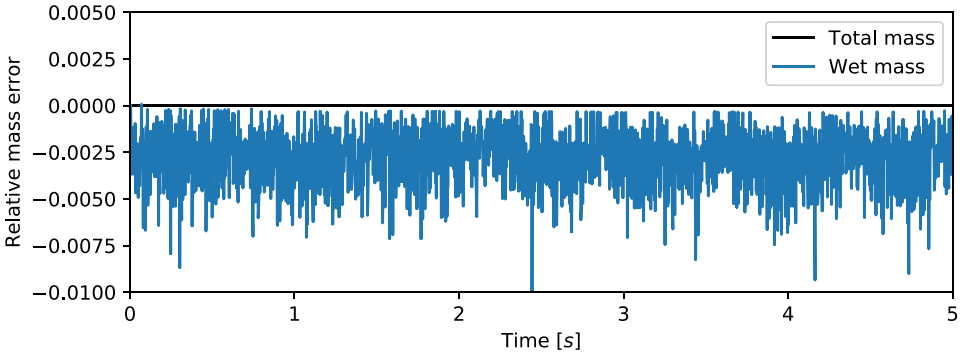

Fig. 11. Parabolic basin. Mass conservation error. The element size used in this simulation is 0.05 m. (For interpretation of the references to colour in this figure legend, the reader is referred to the web version of this article.)

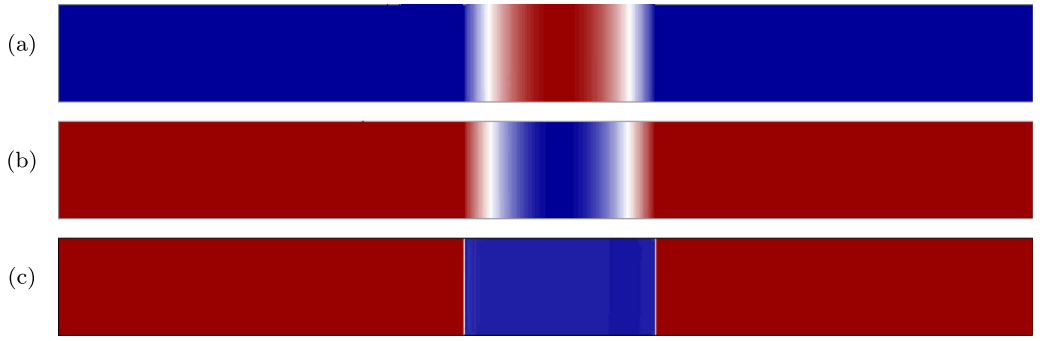

Fig. 12. Parabolic basin. Results with the fine mesh of size 0.01 m at time $t = 1$ s. (a) Water height, (b) x-discharge and (c) x-velocity. There is no legend for simplicity, the red colour is positive and blue means a null or negative magnitude. (For interpretation of the references to colour in this figure legend, the reader is referred to the web version of this article.)

The problem is initialized with the following values:

$$\begin{aligned} h(x,0) &= \max(h_{ex}(100) - z(x), h_{ex}(0)) \\ \mathbf{q}(x,0) &= \mathbf{0} \end{aligned} \tag{49}$$

The Manning coefficient is 0.0328 $\mathrm{m}^{-1/3}\mathrm{s}$ and the water height $h_{ex}(x)$ is a piecewise function defined in [36]. The discontinuity of the water height function is located at $x = 200/3$ m and defines the hydraulic jump. The expression of the stationary exact water depth is:

$$h_{ex} = \begin{cases} \left(\frac{4}{g}\right)^{\frac{1}{3}} \left(\frac{4}{3} - \frac{x}{L}\right) - \frac{9x}{10L}\left(\frac{x}{L} - \frac{2}{3}\right), & \text{for } x < \frac{2L}{3} \\ \left(\frac{4}{g}\right)^{\frac{1}{3}} \left(a_1\left(\frac{x}{L} - \frac{2}{3}\right)^4 + a_1\left(\frac{x}{L} - \frac{2}{3}\right)^3 - a_2\left(\frac{x}{L} - \frac{2}{3}\right)^2 \right. \\ \qquad \left. + a_3\left(\frac{x}{L} - \frac{2}{3}\right) + a_4\right), & \text{for } x \geq \frac{2L}{3} \end{cases} \tag{50}$$

where $a_1 = 0.674202$ m, $a_2 = 21.7112$ m, $a_3 = 14.492$ m, $a_4 = 1.4305$ m and $L = 100$ m. The topography is obtained by a numerical integration using the fourth order Runge Kutta method.

As in the previous example, several meshes are employed and a convergence analysis is performed (Fig. 14). The shock capturing parameter is $\alpha = 1.0$ and we will study the accuracy of the hydraulic jump. Given the initial conditions, the hydraulic jump is generated between the first 50 and 80 s. The overall error is computed at time $t = 200$ s, in order to ensure the stationary state is achieved. The table from Fig. 14 shows the error of the x-discharge over all the domain using the L_2 norm.

Results from different meshes are compared in Figs. 15 and 16. The oscillations are reduced with the finer mesh (Fig. 16), but there is a peak on the discharge at the location of the shock. This peak is initiated because

Fig. 13. Short channel. Geometry of the channel. The vertical line shows the position of the hydraulic jump.

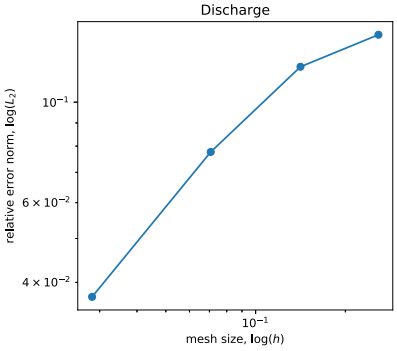

n_{nodes}	Δx	Δt	CFL	$L_2(e_{rel})$
204	2.0	0.005	0.016	0.177
606	1.0	0.005	0.031	0.138
2211	0.5	0.005	0.062	0.088
13026	0.2	0.005	0.15	0.041

Fig. 14. Short channel. Convergence analysis for the x-discharge.

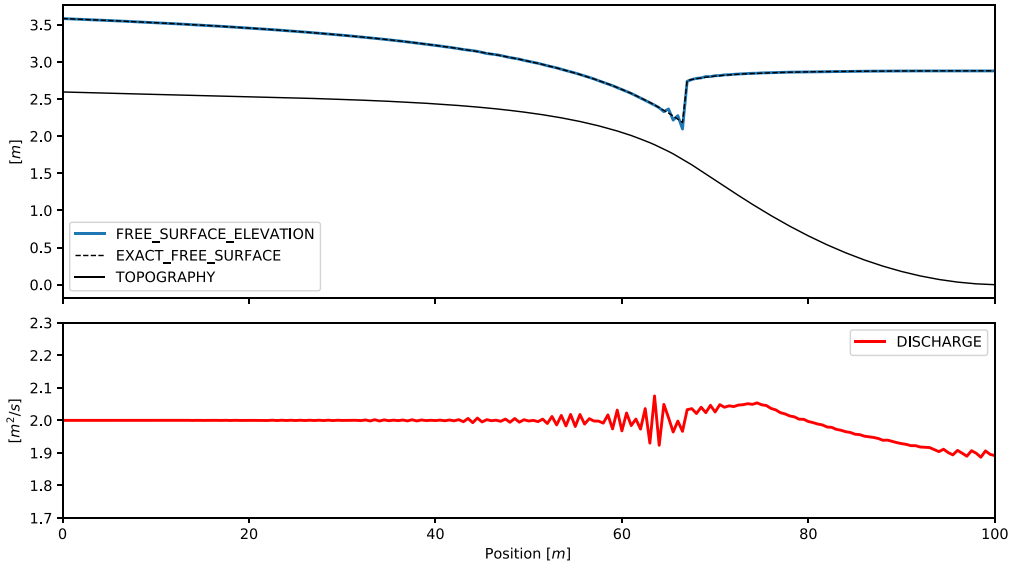

Fig. 15. Short channel. Graph along the cut defined by the center of the channel. The mesh size is 0.5 m.

the momentum balance includes the gradient of the total water depth, and the analytical gradient is a Dirac delta function.

5.4. Experimental dam break flow against an isolated building

The last example consists on the reproduction of the experiment carried out by Soares [38]. A dam break flow with a building downstream is simulated. The problem definition is depicted in Fig. 17. The channel is 3.4 m wide and the end of the dam is located at $x = 0$. As initial conditions, the water depth is set to 0.4 m in the reservoir, while the channel is dry. The Manning coefficient is 0.01 $\mathrm{sm}^{-1/3}$ over all the domain. At the beginning of the simulation, the gate of the dam is removed and the water is allowed to flow around the building.

There are some gauges (Table 1 and Fig. 17) where the water height and velocity are recorded. Experimental data is used to validate the numerical method.

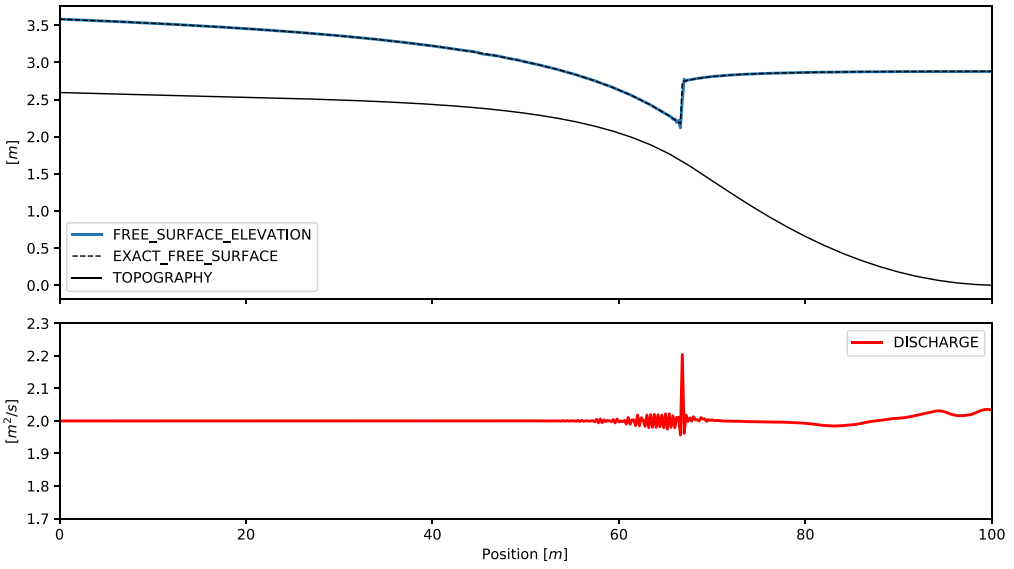

Fig. 16. Short channel. Graph along the cut defined by the center of the channel. The mesh size is 0.2 m.

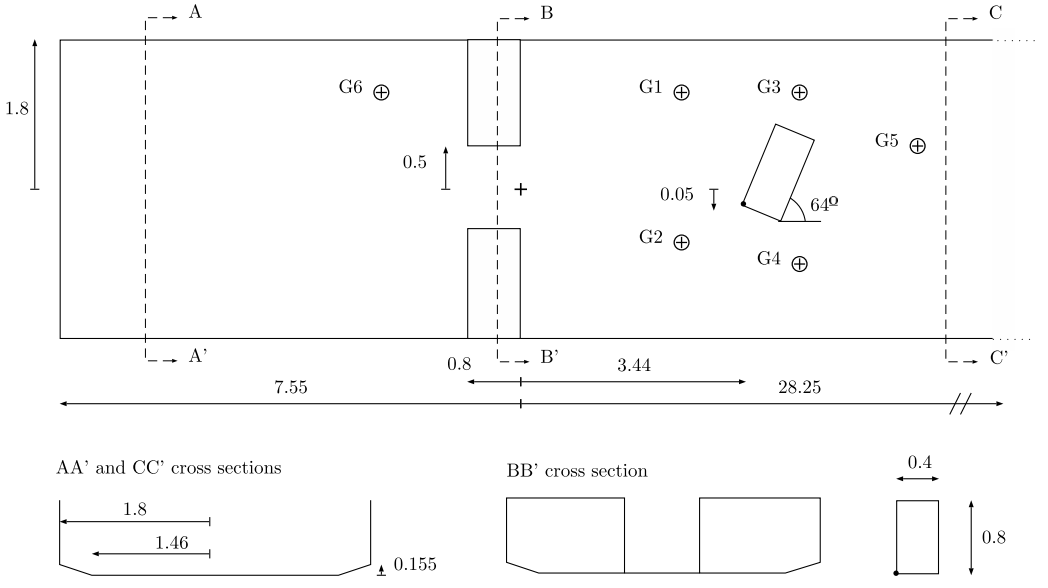

Fig. 17. Experimental dam break flow. Definition of the isolated building benchmark. The dimensions are in m.

Table 1
Experimental dam break flow. Positions of the gauges, units in *m*.

Gauge number	X	Y
1	2.65	1.15
2	2.65	−0.60
3	4.00	1.15
4	4.00	−0.80
5	5.20	0.30
6	−1.87	1.10

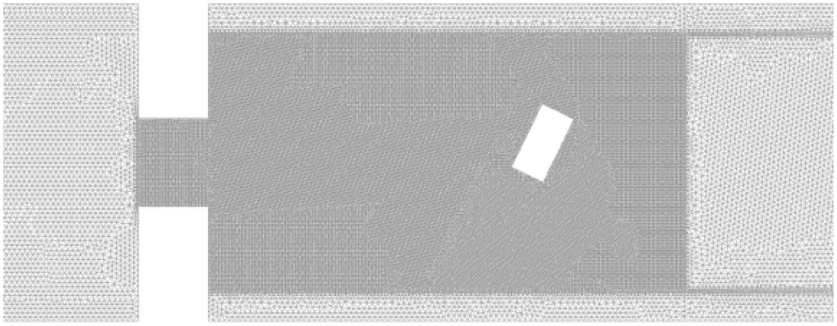

Fig. 18. Experimental dam break flow. Detail of the mesh near the dam and around the building. The coarse elements have an average size of 0.06 m and the refined area has an average element size of 0.02 m. There are 160.000 elements.

The domain is discretized with a mesh with an average element size of 0.05 m. There are 115.000 elements and the time step is computed to keep a courant number of 1.0. Fig. 18 displays two details of the mesh, near the dam and around the building.

To get a general idea of the flow, Fig. 19 shows several results of the water depth after the gate release. Fig. 20 shows the evolution of the water depth at the gauges. An initial delay is observed in the propagation of the front in the gauges 1 to 5.

Gauge 1 is located upstream of the building and close to the left wall of the channel. In gauge 1 there are the main discrepancies between the numerical and experimental results. The vicinity of the wall is responsible for the rapid variations in the water level. After the arrival of the front wave, this is reflected in the wall and a second raise of the water level is observed. About $t = 6$ s, an oblique hydraulic jump is formed and registered in gauge 1. The two first shocks are well captured by the numerical results, but the oblique hydraulic jump is registered latter, at $t = 10$ s, and there is a general overestimation of the ones for the water depth values.

The main hydraulic jump in gauge 2 formed by the reflection against the building is registered at $t = 15$ s, but in the numerical simulation is it formed very rapidly, presenting a discontinuity in time.

Gauge 3 is located at the left hand side of the building, where multiple waves are reflected and practically always it is in subcritical regime. There is a good correlation between numerical and experimental results. Gauge 4 is at the opposite side of the building but the superposition of the reflected waves is more clearly identified. The main discrepancies in the results are concentrated in the first seconds, where the flow is more dynamic.

Gauge 6 is located at the reservoir and registers the superposition of smooth waves during the emptying of the tank.

As stated in [38] there are some difficulties in the recording of the velocity and its validity is discussed. Here we compare only the most representative gauges. Gauge 2 is not fully submerged and the validity of the measurements is good after $t = 14.5$ s. It illustrates the change from supercritical flow to subcritical (Fig. 21). The considerations are similar to the water depth study.

The experimental measurements in gauge 4 (Fig. 22) show a change in the velocity direction around $t = 15$ s due to the rise of water level. The numerical results do not capture this change but the mean and the stationary values are correctly simulated.

In gauge 5 the formation of eddies behind the building can be appreciated from $t = 20$ (Fig. 23). In that case, the experimental results have difficulties to capture the eddies. Results will probably improve by extending the refined region of the mesh. The authors have observed the formation of eddies, but they are not fully developed and its area of influence is not enough to arrive to gauge 5.

In fluid–structure interaction studies, pressure is needed to compute to forces over the structure. The shallow water assumptions drop the dynamic pressures retaining only the hydrostatic ones. In the present case, the pressures are recovered by integrating the hydrostatic pressures given the water depth around the building. However, there is no experimental data about the forces applied to the building and thus, the importance of the dynamic pressures can not be evaluated.

Regarding the performance of the FIC-FEM formulation, it captures the main aspects of the flow, but not the details, since there are some regions on that experiment which violate the shallow water approximations.

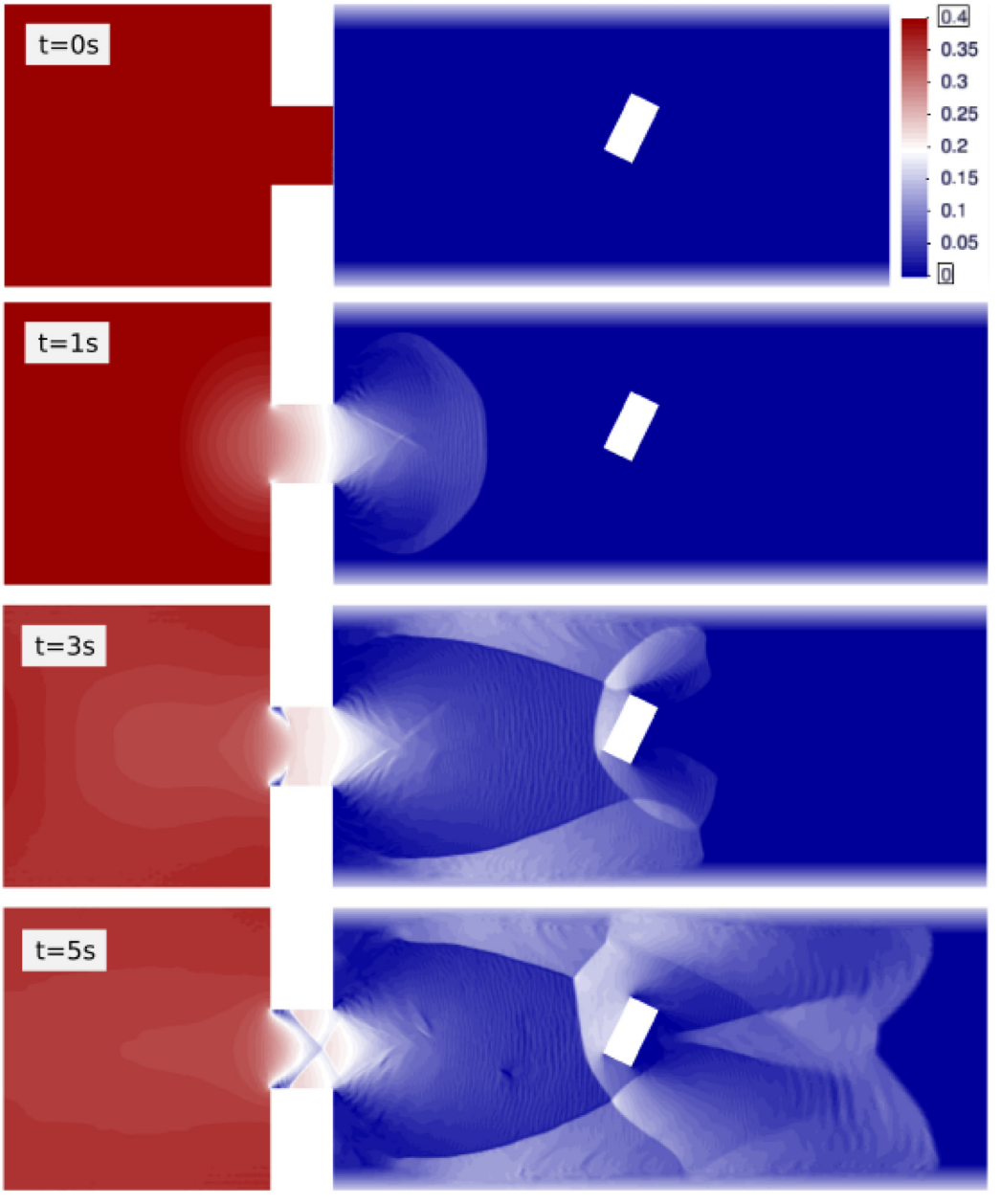

Fig. 19. Experimental dam break flow. Results of the benchmark at times 0, 1 and 3 s.

6. Concluding remarks

We have extended the FIC-FEM procedure to the shallow water equations. Unlike the FIC-based stabilizations for incompressible flows, the present procedure is applied to the coupled mass and momentum balance at the same time using the linearization matrix $\mathbf{A}_i$. It can be seen that this procedure casts to the classical FIC-stabilization for convection diffusion problems, taking the velocity as linearization term. The same procedure can be applied to develop stabilized formulations for compressible flows.

The present extension of the FIC-procedure to the shallow water equations uses the linearization matrix $\mathbf{A}_i$ for the flux terms to project the characteristic length. However, an alternative framework can be explored with the ASGS [15,39] formulation, which includes the linearization matrices of the viscous terms and reaction terms. Since

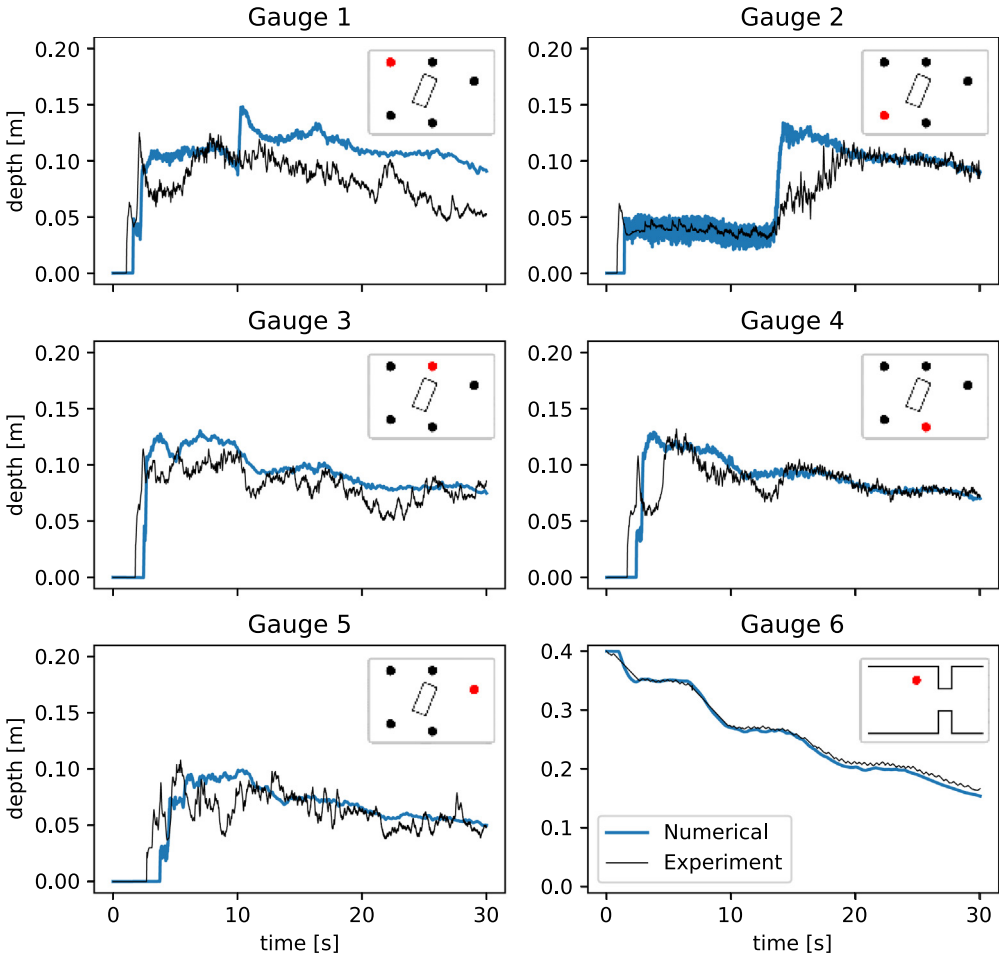

Fig. 20. Experimental dam break flow. Comparison between the obtained water depth with the reference data.

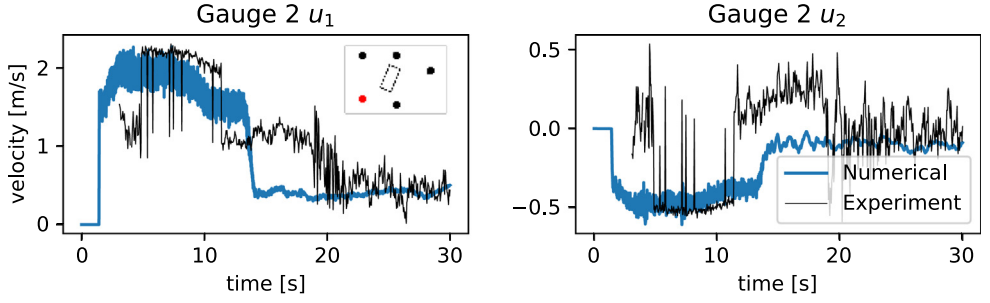

Fig. 21. Experimental dam break flow. Comparison of velocity at gauge 2.

the shallow water equations are dominated by the convective matrix $\mathbf{A}_i$, and thus are strictly hyperbolic, the present stabilization is enough to provide stability, as shown in Section 5.

The present stabilization provides two algorithmic constants, one for the global stabilization and other one for the shock capturing term. From our numerical experiments, we have chosen $\beta = 0.01$ for the stabilization and $\alpha = 1.0$ for the shock capturing.

Regarding the accuracy of the shock capturing and the dry domain model, one must notice that this method is not monotonic. Therefore, like in many other stabilized methods, the order of convergence is dropped around

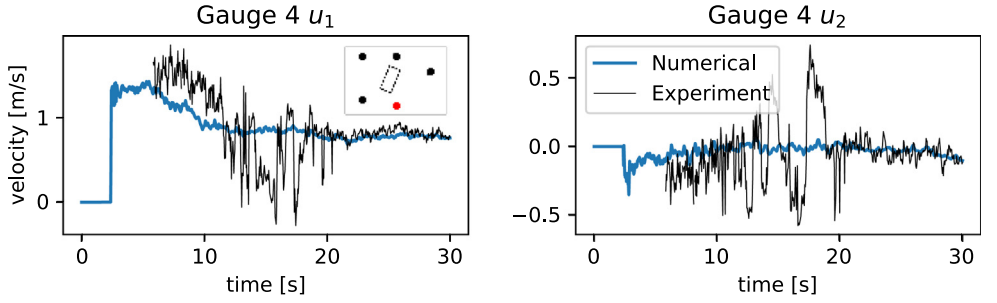

Fig. 22. Experimental dam break flow. Comparison of velocity at gauge 4.

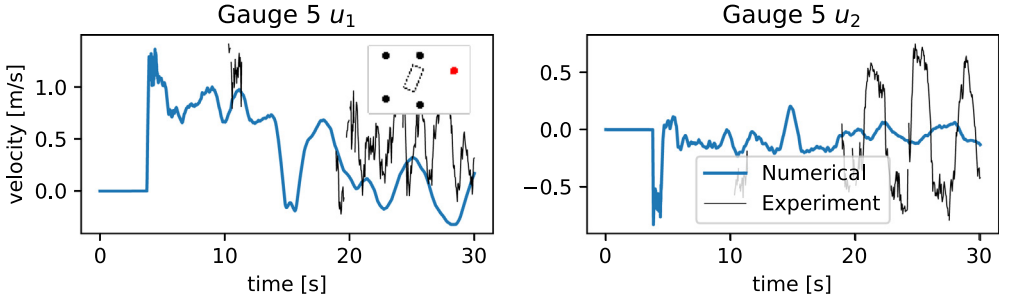

Fig. 23. Experimental dam break flow. Comparison of velocity at gauge 5.

discontinuities such as hydraulic jumps and the shoreline. However, the spurious oscillations, specially the oscillations related to the moving shoreline, are bounded and the method is globally mass preserving.

The present FIC-FEM procedure has produced accurate results for the examples considered. In the first example, the artificial diffusion is evaluated and it has been proved to be small and practically inappreciable. The shock capturing term allows to solve supercritical problems with discontinuities and the present procedure is also able to deal with partially wet domains. Finally, a numerical simulation of a dam break flow against an isolated building is performed. The limitations of the model essentially come from the shallow water equations hypothesis. In fact, the last example presents local regions where the dynamic pressure is not negligible. It is not an obstacle to simulate the main aspects of the flow and the numerical results are in good agreement with the experimental data.

Declaration of competing interest

The authors declare that they have no known competing financial interests or personal relationships that could have appeared to influence the work reported in this paper.

Acknowledgments

The first author gratefully acknowledges the Universitat Politècnica de Catalunya and Banco Santander for the financial support for his pre-doctoral grant (53 FPI-UPC 2018). This research was partially funded by the project PARAFLUIDS (PID2019-104528RB-I00). The authors also acknowledge the financial support from the CERCA programme of the Generalitat de Catalunya, Spain, and from the Spanish Ministry of Economy and Competitiveness, through the "Severo Ochoa Programme for Centres of Excellence in R&D", Spain (CEX2018-000797-S).

Appendix

The stabilization matrices are the result of multiplying $\mathbf{A}$ tensor by itself:

$$\mathbf{A}_1\mathbf{A}_1 = \begin{pmatrix} 3u_1^2 + c^2 & 0 & -2u_1^3 + 2u_1c^2 \\ 2u_1u_2 & u_1^2 & -2u_1^2u_2 + u_2c^2 \\ 2u_1 & 0 & -u_1^2 + c^2 \end{pmatrix} \tag{51a}$$

$$\mathbf{A}_2\mathbf{A}_2 = \begin{pmatrix} u_2^2 & 2u_1u_2 & -2u_1u_2^2 + u_1c^2 \\ 0 & 3u_2^2 + c^2 & -2u_2^3 + 2u_2c^2 \\ 0 & 2u_2 & -u_2^2 + c^2 \end{pmatrix} \tag{51b}$$

$$\mathbf{A}_1\mathbf{A}_2 = \begin{pmatrix} 2u_1u_2 & u_1^2 + c^2 & -2u_1^2u_2 \\ u_2^2 & 2u_1u_2 & -2u_1u_2^2 + u_1c^2 \\ u_2 & u_1 & -u_1u_2 \end{pmatrix} \tag{51c}$$

$$\mathbf{A}_2\mathbf{A}_1 = \begin{pmatrix} 2u_1u_2 & u_1^2 & -2u_1^2u_2 + u_2c^2 \\ u_2^2 + c^2 & 2u_1u_2 & -2u_1u_2^2 \\ u_2 & u_1 & -u_1u_2 \end{pmatrix} \tag{51d}$$

References

[1] O.C. Zienkiewicz, R.L. Taylor, Finite Element Method: Fluid dynamics, Vol. 3, fifth ed., Butterworth-Heinemann, 2000.
[2] I. Navon, Finite-element simulation of the shallow-water equations model on a limited-area domain, Appl. Math. Model. 3 (5) (1979) 337–348, http://dx.doi.org/10.1016/S0307-904X(79)80040-2.
[3] I.M. Navon, A review of finite-element methods for solving the shallow-water equations, Comput. Modelling Ocean Eng. (1988) 273–278.
[4] P. Hood, C. Taylor, Navier Stokes Equations using Mixed Interpolation. Finite-Element Methods in Flow Problems, Huntsville Press, 1974.
[5] P. Ortiz, Non-oscillatory continuous FEM for transport and shallow water flows, Comput. Methods Appl. Mech. Engrg. s 223–224 (2012) 55–69, http://dx.doi.org/10.1016/j.cma.2012.02.022.
[6] V. Ambati, O. Bokhove, Space–time discontinuous Galerkin finite element method for shallow water flows, J. Comput. Appl. Math. 204 (2) (2007) 452–462, http://dx.doi.org/10.1016/j.cam.2006.01.047, Special Issue: The Seventh International Conference on Mathematical and Numerical Aspects of Waves (WAVES'05).
[7] A.A. Khan, W. Lai, Modeling Shallow Water Flows using the Discontinuous Galerkin Method, first ed., CRC Press, 2014.
[8] H. Lee, Implicit discontinuous Galerkin scheme for shallow water equations, J. Mech. Sci. Technol. 33 (2019) http://dx.doi.org/10.1007/s12206-019-0625-2.
[9] A. Brooks, T. Hughes, Streamline Upwind/Petrov-Galerkin formulations for convective dominated flows with particular emphasis on the incompressible Navier-Stokes equations, Comput. Methods Appl. Mech. Eng. (1982).
[10] R. Codina, Comparison of some finite element methods for solving the diffusion-convection-reaction equation, Comput. Methods Appl. Mech. Engrg. 156 (1) (1998) 185–210, http://dx.doi.org/10.1016/S0045-7825(97)00206-5.
[11] T.J. Hughes, L.P. Franca, G.M. Hulbert, A new finite element formulation for computational fluid dynamics: VIII. The Galerkin/least-squares method for advective-diffusive equations, Comput. Methods Appl. Mech. Engrg. 73 (2) (1989) 173–189.
[12] E. Oñate, S. Idelsohn, O.C. Zienkiewicz, R.L. Taylor, A finite point method in computational mechanics. Applications to convective transport and fluid flow, Internat. J. Numer. Methods Engrg. 39 (22) (1996) 3839–3866, http://dx.doi.org/10.1002/(SICI)1097-0207(19961130)39:22<3839::AID-NME27>3.0.CO;2-R.
[13] E. Oñate, Derivation of stabilized equations for numerical solution of advective-diffusive transport and fluid flow problems, Comput. Methods Appl. Mech. Engrg. 151 (1) (1998) 233–265, http://dx.doi.org/10.1016/S0045-7825(97)00119-9, Containing papers presented at the Symposium on Advances in Computational Mechanics.
[14] E. Oñate, Possibilities of finite calculus in computational mechanics, Internat. J. Numer. Methods Engrg. 60 (1) (2004) 255–281, http://dx.doi.org/10.1002/nme.961.
[15] R. Codina, Finite element approximation of the hyperbolic wave equation in mixed form, Comput. Methods Appl. Mech. Engrg. 197 (13) (2008) http://dx.doi.org/10.1016/j.cma.2007.11.006.
[16] T.J. Hughes, M. Mallet, A new finite element formulation for computational fluid dynamics: IV. A discontinuity-capturing operator for multidimensional advective-diffusive systems, Comput. Methods Appl. Mech. Engrg. 58 (3) (1986) 329–336.
[17] R. Codina, Finite element approximation of the convection-diffusion equation: Subgrid-scale spaces, local instabilities and anisotropic space-time discretizations, in: C. Clavero, J.L. Gracia, F.J. Lisbona (Eds.), BAIL 2010 - Boundary and Interior Layers, Computational and Asymptotic Methods, Springer Berlin Heidelberg, Berlin, Heidelberg, 2011, pp. 85–97, http://dx.doi.org/10.1007/978-3-642-19665-2_10.
[18] J. Cotela-Dalmau, R. Rossi, E. Oñate, A FIC-based stabilized finite element formulation for turbulent flows, Comput. Methods Appl. Mech. Engrg. 315 (2016) http://dx.doi.org/10.1016/j.cma.2016.11.020.
[19] M. Leclerc, J.-F. cois Bellemare, G. Dumas, G. Dhatt, A finite element model of estuarian and river flows with moving boundaries, Adv. Water Resour. 13 (4) (1990) 158–168.
[20] M. Heniche, Y. Secretan, P. Boudreau, M. Leclerc, A two-dimensional finite element drying-wetting shallow water model for rivers and estuaries, Adv. Water Resour. 23 (4) (2000) 359–372, http://dx.doi.org/10.1016/S0309-1708(99)00031-7.
[21] A.S. Candy, An implicit wetting and drying approach for non-hydrostatic baroclinic flows in high aspect ratio domains, Adv. Water Resour. 102 (2017) 188–205, http://dx.doi.org/10.1016/j.advwatres.2017.02.004.
[22] M.L.C. Barros, P.C.C. Rosman, J.C.F. Telles, J.P.S. Azevedo, A simple wetting and drying method for shallow water flow with application in the Vitória Bay estuary, Brazil, in: Water Resources Management VI, Vol. 145, 2011, pp. 215–225, http://dx.doi.org/10.2495/WRM110181.

[23] A. Defina, Two-dimensional shallow flow equations for partially dry areas, Water Resour. Res.- WATER RESOUR. RES. 36 (2000) http://dx.doi.org/10.1029/2000WR900167.
[24] M.B. Abbott, Computational Hydraulics : Elements of the Theory of Free Surface Flows / M.B. Abbott, Belmont, Calif, Pitman Pub. ; Fearon-Pitman Publishers London, 1979, p. xviii, 324.
[25] V.T. Chow, D.R. Maidment, L.W. May, Applied Hydrology, in: McGraw-Hill Series in Water Resources and Environmental Engineering, McGraw-Hill Book Company, New York, 1988.
[26] E.B. Castellet, Modelación del flujo en lámina libre sobre cauces naturales. Análisis integrado con esquemas en volúmenes finitos en una y dos mensiones (Ph.D. thesis), Universitat Politécnica de Catalunya, 2005.
[27] P.-A. Raviart, E. Godlewski, Numerical Approximation of Hyperbolic Systems of Conservation Laws, in: Applied Mathematical Sciences, vol. 118, Springer, New York, NY, 1996.
[28] R. Codina, J.M. González-Ondina, G. Díaz-Hernández, J. Principe, Finite element approximation of the modified Boussinesq equations using a stabilized formulation, Internat. J. Numer. Methods Fluids 57 (9) (2008) 1249–1268, http://dx.doi.org/10.1002/fld.1718.
[29] M. Bercovier, O. Pironneau, Error estimates for finite element method solution of the Stokes problem in the primitive variables, Numer. Math. 33 (1979) 211–224.
[30] C.F. Curtiss, J.O. Hirschfelder, Integration of stiff equations, Proc. Natl. Acad. Sci. USA 38 (3) (1952) 235–243, http://dx.doi.org/10.1073/pnas.38.3.235.
[31] R. Brayton, F. Gustavson, G. Hachtel, A new efficient algorithm for solving differential-algebraic systems using implicit backward differentiation formulas, Proc. IEEE 60 (1) (1972) 98–108, http://dx.doi.org/10.1109/PROC.1972.8562.
[32] A. Kurganov, G. Petrova, A second-order well-balanced positivity preserving central-upwind scheme for the Saint-Venant system, Commun. Math. Sci. 5 (2007) http://dx.doi.org/10.4310/CMS.2007.v5.n1.a6.
[33] S. Badia, A. Hierro, On monotonicity-preserving stabilized finite element approximations of transport problems, SIAM J. Sci. Comput. 36 (6) (2014) http://dx.doi.org/10.1137/130927206.
[34] P. Dadvand, R. Rossi, E. Oñate, An object-oriented environment for developing finite element codes for multi-disciplinary applications, Arch. Comput. Methods Eng. 17 (3) (2010).
[35] P. Dadvand, R. Rossi, M. Gil, X. Martorell, J. Cotela, E. Juanpere, S. Idelsohn, E.O. nate, Migration of a generic multi-physics framework to HPC environments, Comput. & Fluids 80 (2013).
[36] O. Delestre, C. Lucas, P.-A. Ksinant, F. Darboux, C. Laguerre, T.-N.-T. Vo, F. James, S. Cordier, SWASHES: A compilation of shallow water analytic solutions for hydraulic and environmental studies, Internat. J. Numer. Methods Fluids 72 (2013) 269–300, http://dx.doi.org/10.1002/fld.3741, arXiv:1110.0288.
[37] I. MacDonald, M.J. Baines, N.K. Nichols, P.G. Samuels, Analytic benchmark solutions for open-channel flows, J. Hydraul. Eng. 123 (11) (1997) 1041–1045, http://dx.doi.org/10.1061/(ASCE)0733-9429(1997)123:11(1041).
[38] S.S.-F. ao, Y. Zech, Experimental study of dam-break flow against an isolated obstacle, J. Hydraul. Res. 45 (sup1) (2007) 27–36, http://dx.doi.org/10.1080/00221686.2007.9521830.
[39] T.J. Hughes, Multiscale phenomena: Green's functions, the Dirichlet-to-Neumann formulation, subgrid scale models, bubbles and the origins of stabilized methods, Comput. Methods Appl. Mech. Engrg. 127 (1) (1995) 387–401.